

OPEN ACCESS

EDITED BY

Wenfeng Xia,
King's College London, United Kingdom

REVIEWED BY

Ilya Pyatnitskiy,
The University of Texas at Austin, United States
Ammar A. Oglat,
Hashemite University, Jordan

*CORRESPONDENCE

Chatsuda Songsaeng,
✉ n12102201@students.meduniwien.ac.at

RECEIVED 28 June 2024

ACCEPTED 30 October 2024

PUBLISHED 20 November 2024

CITATION

Songaeng C, Köhrer J, Ortner M, Zalka L,
Salomon E, Huber S, Homolka P, Kollmann C,
Figl M and Hummel J (2024) A phantom study
on the applicability of a detectability index in
ultrasound imaging.
Front. Phys. 12:1456478.
doi: 10.3389/fphy.2024.1456478

COPYRIGHT

© 2024 Songsaeng, Köhrer, Ortner, Zalka,
Salomon, Huber, Homolka, Kollmann, Figl and
Hummel. This is an open-access article
distributed under the terms of the [Creative
Commons Attribution License \(CC BY\)](#). The
use, distribution or reproduction in other
forums is permitted, provided the original
author(s) and the copyright owner(s) are
credited and that the original publication in
this journal is cited, in accordance with
accepted academic practice. No use,
distribution or reproduction is permitted
which does not comply with these terms.

A phantom study on the applicability of a detectability index in ultrasound imaging

Chatsuda Songsaeng^{1,2*}, Johannes Köhrer^{1,2}, Markus Ortner¹,
Lukas Zalka^{1,2}, Elisabeth Salomon¹, Sten Huber¹,
Peter Homolka¹, Christian Kollmann¹, Michael Figl^{1,2} and
Johann Hummel^{1,2,3}

¹Center for Medical Physics and Biomedical Engineering, Medical University of Vienna, Spitalgasse, Vienna, Austria, ²Christian Doppler Laboratory for Mathematical Modelling and Simulation of Next-Generation Medical Ultrasound Devices, Vienna, Austria, ³Christian Doppler Laboratory for Patient-Centered Breast Imaging, Vienna, Austria

The assessment of clinical image quality on ultrasound is currently often *subjective*. While image quality factors such as contrast response or depth of penetration can be evaluated semi-automatically, the evaluation of high contrast resolution requires test objects with specific inserts. The aim of this study was to evaluate the applicability of image quality metrics which were derived from Linear System Theory in the field of medical ultrasound imaging. Modular Transfer Function (MTF) and noise power spectrum (NPS) were determined on four phantoms. Image quality was assessed using a detectability index for different diameters. One phantom contained a cylinder filled with water, which appears as a circle in the US images. The other three phantoms were homogeneous and consisted of three different materials all based on PVA (polyvinyl alcohol). The basic phantom material was a 10% PVA hydrogel. The two other materials included microplastic spheres and starch to increase echogeneity. NPS and the MTF were determined using MATLAB routines. Two linear US transducers with bandwidths of 2.4–10 and 4–15 MHz were used to show the dependence of the index on the principal frequency of the US wave. The results show that for all phantom materials and object sizes (1–10 mm diameter), the detectability indices decreased with increasing penetration depth (from 6 to 10 cm). In addition, all indices of the higher frequency transducer were higher than those of the lower frequency transducer. When comparing the different phantom materials (PVA, PVA with starch and PVA with microspheres), different mean pixel value (MPV) were found, while the standard deviations for the materials were similar. This enabled us to evaluate the detectability index at different signal-to-noise ratios (SNR). Measures of image homogeneity (coefficient of the variance and variation) showed no significant difference to a commercial phantom (*p*-values ranging from 0.16 to 1, average *p*-value 0.5). These results suggest that the concept of a detectability index can also be applied to US imaging.

KEYWORDS

ultrasound phantom, microcapsule, modulation transfer function, noise power spectrum, detectability index

1 Introduction

Ultrasound has a wide range of applications and is a valuable tool for doctors in a variety of medical specialties [1]. Diagnostic US is commonly used to monitor fetal development during pregnancy (gynecology), visualize abdominal organs (abdominal imaging), diagnose heart disease (echocardiography) and assess blood vessels (Doppler and vascular imaging) [2, 3]. The most critical component of US equipment is the transducer, which both emits and receives US waves by converting electrical signals into sound waves [4]. Transducers come in different types, each suitable for the specific application, e.g., convex (curvilinear), linear, and intercavity transducers [5]. Convex transducers provide a wide field of view commonly used in abdominal imaging. Linear transducers provide high resolution images often used in vascular examinations [6].

Quality Assurance (QA) is essential in maintaining the optimal image quality of US devices, ensuring compliance with manufacturers' guidelines and regulatory and accreditation agency standards [7, 8].

Currently, the assessment of clinical image quality on US is mostly *subjective* because objective criteria for assessing clinical image quality have not been fully developed and accepted [9]. While image quality factors such as contrast response or depth of penetration can be evaluated semi-automatically by software [10], the evaluation of high contrast resolution requires test objects with specific inserts, where the observer has to decide which of these inserts are still visible [11, 12]. Such test objects are essential tools for assessing the image quality of US equipment [13]. In particular, tissue-mimicking phantoms designed to replicate the properties of human tissues are crucial for the validation of imaging techniques used in quality control and clinical training [14].

However, there are several disadvantages associated with the use of subjective QA [7]. The results show high variance due to different observers (objectivity), and from the same observer on different observations (reproducibility) [15, 16]. As a result, 'manual' evaluation of such images is time consuming, especially considering the low reproducibility that requires a series of images. This problem is also known from other modalities, notably radiodiagnostics [17]. Here, this limitation has been addressed with the introduction of image metrics such as MTF and NPS. These metrics can be used to mathematically derive a specific diameter or thickness that is still visible. Unfortunately, the direct application of these methods to US is limited by the non-linear nature of US images.

In [18], a mathematical framework was introduced indicating that the translation variance of US images is mainly in the axial direction. The absence of directional dependence can be replaced by the local translation invariance, which can be used for linear image metrics within certain lines parallel to the line of piezo elements of the transducer. An interpolation between the measured lines could allow for a global application of the image metrics to the interesting part of the US image.

The computation of MTF and NPS enables the derivation of a detectability index, as discussed in [19, 20]. This index correlates with the ability to detect objects of varying sizes. Essentially, it provides an insight into which contrasts remain perceptible to human observers at certain object sizes, or, conversely, which object sizes remain perceptible at certain contrasts. In US, such an index could be used to assess lesions of different types, which are depicted

as circular or ellipsoidal shapes in the US image plane. This includes lesions such as cysts and tubular anomalies of different sizes, which are crucial for the diagnostic interpretation of US images. Therefore, this quality assessment method is relevant to a wide range of clinical applications beyond specific diagnostic questions. Hence, this QA approach would apply to broad clinical areas and is not limited to a specific clinical question [21, 22].

In this paper, we present measurements of such an index for two different types of US transducers types. Several phantom materials were used for the background noise, including a novel phantom material containing micro spheres that may facilitate the generation of specific structured noise characteristics.

Based on the findings by Ng et al. [18] suggesting the possible usability of a detectability index in Ultrasound imaging, despite it violating the conditions of a linear shift-invariant system, we evaluated its practical applicability. The feasibility of a detectability index, which is well established in radio-diagnostics was thus tested in the field of US imaging. The MTF was measured using an established method by [23, 24]. As the spatial resolution of US images depends on the frequency used, we calculated the index for different penetration depths with transducers operating at different main frequencies.

A preliminary version introducing some concepts was presented at the SPIE Medical Imaging Conference 2024 [25].

2 Methods

2.1 Phantom fabrication

2.1.1 Phantom base material

The ultrasound phantoms used PVA (polyvinyl alcohol) as the base material, a synthetic polymer commonly utilized in tissue-like phantoms. The production protocol followed the procedures described in [26] and [23].

We produced three homogeneous phantom materials using three different materials: PVA, PVA with starch, and PVA with microcapsules. For the MTF phantom which contains an empty cylinder, that appears as a circle in the ultrasound image, we also used PVA with starch. The phantom with different materials is shown in Figure 1.

For all materials, 10% PVA powder (degree of hydrolysis greater than 99 percent, average molecular weight 85,000 to 124,000, Sigma-Aldrich, St. Louis, MO, United States catalog nr 363146) was mixed into demineralized water. To prevent bacteria and fungal inversion, we add 0.2% methyl-4-hydroxybenzoate (Sigma-Aldrich, Karnataka, India).

2.1.2 PVA hydrogel preparation

The phantom base material was continuously mixed at 253 rpm at 85°C until the PVA was completely dissolved. The mixing temperature was carefully monitored with a thermometer keeping the temperature range between 75°C and 85°C. After mixing the solution for 2 hours, the solution was cooled down to room temperature. The viscosity of the mixture was similar to that of honey. The solution was reheated in an oven for 60 min at 85°C to remove air bubbles [27].

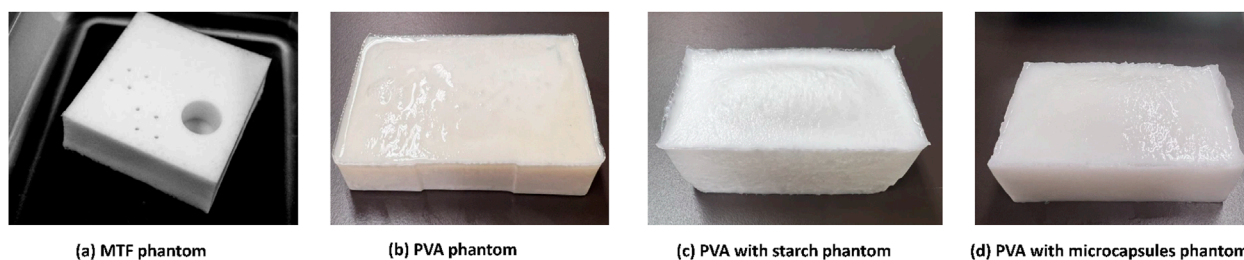


FIGURE 1
The US phantoms used: (A) MTF phantom, (B) PVA phantom, (C) PVA with starch phantom, and (D) PVA with microcapsules phantom.

For the PVA with starch phantom material, we added 1% lab starch (Sigma-Aldrich, St. Quentin, Fallavier, France) to the phantom base material, which introduced additional background scatter and increased attenuation.

For the PVA-microcapsule phantom, we added 1% core-shell microcapsules filled with silicone oil (with a viscosity of 10 cSt) to the phantom base material and surrounded by a polymer shell made of UV-curable resin. These microcapsules were included to enhance background scatter [28] and increase attenuation in the US image [29]. The core-shell microcapsules were created by mixing resin, silicone oil, and 1% PVA in a water solution at 10,000–20,000 rpm for 2 min. This mixture was then exposed to UV light for 5 min to harden the polymer shell, following the bulk emulsion method as described in [30, 31]. The PVA-microcapsule mixture was stirred at room temperature until the solution was completely dissolved.

2.1.3 Phantom freeze-thaw-cycles

Once the solutions cooled to room temperature, they were poured into a PMMA mould. The four phantoms were then placed in a refrigerator at -20°C for 20-hour freezing periods. After that, they were returned to the $+6^{\circ}\text{C}$ refrigerator for 20 h (1 freeze-thaw cycle = 40 h). After thawing, the phantoms were stored in water permanently to avoid shrinking and deformations. The PVA and PVA with starch phantom materials were subjected to four freeze-thaw cycles, PVA with microcapsules to one freeze-thaw cycle. In a freeze-thaw cycle the properties of PVA hydrogels are significantly affected by the gelation parameters. More gelation points lead to a stronger gel with increased cross-linking density and homogeneity of the phantoms. As the number of freeze-thaw cycles increases, more PVA chains are driven towards polymer-rich regions, leading to enhanced crystallization and gelation processes, which affect the homogeneity of the ultrasound phantom [32]. The number of freeze-thaw cycles was chosen to achieve a satisfactory homogeneity of the phantom material. The phantom fabrication process, the freeze-thaw procedure and the US image acquisition is shown in Figure 2.

2.2 Ultrasound transducers

A GE Voluson E6 US system was used (General Electric, United States, Chicago, Illinois), equipped with two GE multi-frequency linear transducers: the 9L-D with a bandwidth of 2.4–10 MHz (transducer 1) and an ML6-15-D with a bandwidth of 4–15 MHz

(transducer 2). Both transducers were operated at their regular frequency. The grey level function was set to 1 (linear relationship), and all filters (colour, line, enhance and reject) were disabled. Persistence (the averaging of a series of images to eliminate artefacts) was set to the maximum value of eight. The gain was maintained at a constant value ($G_n = 0$) for all images. Dynamic and focus were set to 1. During the imaging, we varied the depth of penetration (6, 8, and 10 cm) in both transducers. This approach permitted the assessment and comparison of image quality and penetration capabilities across varying depths.

2.3 Determination of the MTF

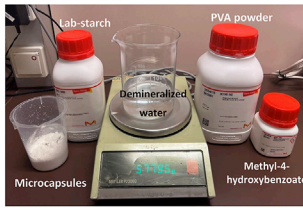
The phantom used for the MTF measurement was made of PVA with starch material and had a hollow cylinder that filled with water when the phantom was immersed in water. This cylinder appeared as a circle in the ultrasound images.

The process of determining the MTF was according to the method described by Kaar et al. [23] and, more recently, by Strocchi et al. [24]. Initially, the user selects a rectangular area containing the cylindrical target together with a surrounding area of appropriate size. Subsequently, this area is automatically cropped to form a square region. A roll-out procedure (see Figure 3) is then applied, which rotates the image and extracts a line of pixels. The boundary between the high and low intensity regions is then determined. Due to the elasticity of our specific US phantom and potential image distortion, this boundary is not a perfect circle. For each pixel line in the unrolled image, a derivative of the grey values is calculated. The minimum of this derivative is taken as a point on the boundary between the light and dark areas. The pixel lines are then shifted in order to have the intensity leap at the same vertical position. To refine this vertical line, we apply a smoothing algorithm that also eliminates outliers. This is achieved by local regression using weighted linear least squares and a second-degree polynomial model. The MTF is then derived from the Edge Spread Function [33].

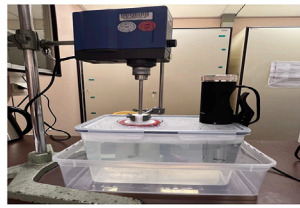
2.4 Determination of normalized noise power spectrum (NNPS)

The NPS was determined using a modified Matlab function referenced by [34]. A region of interest (ROI) of size $145 \times$

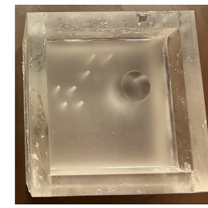
Step1: Weighted and added 10%PVA, 1%starch, 1%microcapsules, 0.2%methyl-4-hydroxybenzoate and demineralized water into the beaker.



Step2: Mixed the ingredients over 85 °C at 253 rpm. for for 2 hrs.



Step3: After cooled to room temperature, the solution were poured into a PMMA mould.



Step4: The phantoms were placed in a refrigerator at -20°C for 20-hour freezing periods.



Step5: Phantoms were returned to the +6°C refrigerator for 20 hours for thawing



Step6: Checked the US images of the phantoms.



FIGURE 2 The phantom fabrication process, the freeze-thaw procedure and the US image acquisition.



FIGURE 3 Determination of MTF. On the left-hand side, the image of the cylinder is displayed together with the manually defined ROI. Within this ROI, the boundary of the circle is automatically detected and then rolled out and shifted (left side).



145 pixels (see Figure 4) was manually positioned in the US image, with 25 sub-images extracted at dimensions of 48 × 48 pixels within this ROI. NPS calculations were performed for each sub-ROI average and multiplied by a Hann tapering filter. Finally, the 2-dimensional symmetric NPS was converted from Cartesian to radial coordinates and normalized by dividing the NPS by the squared mean pixel value of the ROI (=NNPS). The flow chart of MTF and NNPS calculation is shown in Figure 5.

2.5 Detectability index d'

Finally, the detectability index d' as a measure of image quality was calculated by [20].

$$d' = \frac{\sqrt{2\pi}C \int S^2(u)MTF^2(u)VTF^2(u)udu}{\sqrt{\int S^2(u)MTF^2(u)VTF^4(u)NNPS(u)udu}} \tag{1}$$

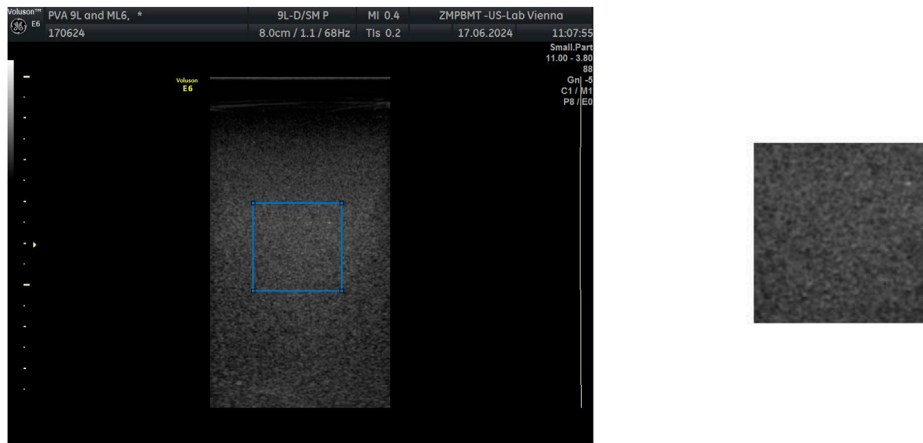


FIGURE 4
Determination of NPS. The right image shows the cropped ROI from the original US image (left).

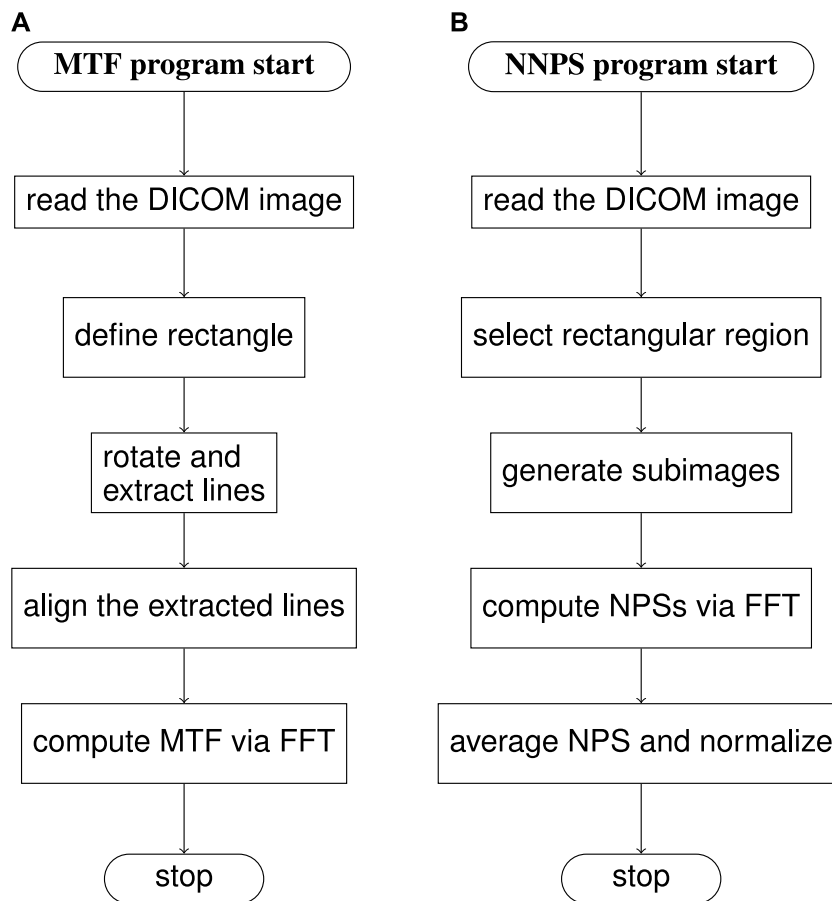


FIGURE 5
The flowchart of the MTF and NPS calculation process. The left image (A) shows the MTF calculation process and the right image (B) shows the NPS calculation process.

The equation can be split up into two parts, the relative contrast C , which is independent of the size of the object (i.e., the contrast for large objects) and the size dependent factor κ

including all the image metrics defined in the frequency space. Therefore, Equation 1 can be written as

$$d' = C \cdot \kappa \tag{2}$$

with

$$\kappa = \frac{\sqrt{2\pi} \int S^2(u) MTF^2(u) VTF^2(u) u du}{\sqrt{\int S^2(u) MTF^2(u) VTF^4(u) NNPS(u) u du}}. \quad (3)$$

The signal spectrum S for the discs of different diameters was defined by the first-order Bessel function of the first kind. The relative contrast was determined by measuring the mean pixel value (MPV) of the background and an anechoic target: $C = (MPV_{background} - MPV_{target}) / MPV_{background}$. For the sake of simplicity, the MPV of the anechoic target was set to zero. Consequently, the index d' is reduced to κ .

The visual transfer function (VTF) representing the contrast sensitivity of the human eye and the visualisation conditions is given in a functional form by

$$VTF(u_c) = k_1 u_c^2 \exp(-u_c/k_2),$$

where u_c is the spatial frequency in cycle/degree [35], with $k_1 = 0.605$ and $k_2 = 1.748$ [36]. With a typical viewing distance of 40 cm the VTF curve has been converted to

$$VTF(u) = 29.5 * u^2 \exp(-4u),$$

where u is the spatial frequency in cycles/mm.

2.6 Dependence of the detectability index on the transducer and the penetration depth

We used three different penetration depths for the NNPS measurement (6, 8 and 10 cm). For each depth, the focus was positioned in the middle of the image. The ROIs for determining the NPS were then positioned in the center of the focal range. Detectability indices were then calculated using the resulting NPS with the corresponding MTFs (with respect to penetration depth and frequency). To determine the error bars for the results, we used five MTF and NNPS images and calculated the index independently for each transducer. The error bars shown in the figures correspond to $2 \cdot \sigma$.

2.7 Homogeneity of three phantom materials

In ultrasound QA it is common to evaluate the homogeneity (or uniformity) simply visually [37, 38]. To calculate and compare the homogeneity of the phantoms we applied methods previously described by [39]. Here, the variation and standard deviation of the background-signal-to-noise ratio (bSNR) are calculated. These are determined from regions of interest that are shifted over the region of assumed uniformity. For this purpose, six square ROIs of equal length were defined at two focus distances from the US probes. These squares were systematically moved with a step size equal to half of their length, while maintaining a roughly 20-pixel margin from both the left and right sides of the

image and the mean pixel value (MPV) within each ROIs was determined. Three different penetration depths were applied (6, 8, and 10 cm). For each depth and focus position, the mean bSNR, the standard deviation of the bSNRs and the coefficient of the variance ($Cov = \sigma_{bSNR} / mean_{bSNR}$) were calculated. In addition, the variation was determined as defined in the EUREF protocol [39] by $(max_{bSNR} - min_{bSNR}) / min_{bSNR}$. These numbers were then compared with the results of an evaluation of a commercial reference phantom (ATS-550 phantom, ATS Laboratories, Bridgeport, CT, United States).

3 Results

3.1 The detectability index d'

Figure 6 illustrates the detectability indices corresponding to the homogeneous phantom made of pure PVA and three penetration depths for object sizes of 1–10 mm. ROIs were positioned at two distances from the scan head (top and middle). Detectability indices decreased consistently across all phantom materials and object diameters with increasing penetration depth (6–10 cm) for both transducer types. Furthermore, the detectability indices increased with increasing object diameter (1, 2, 3, 4, 5, 6, 8, 10 mm) for both transducer types. Figure 7 displays the corresponding indices for the phantom made of PVA and micro-particles, Figure 8 shows the results for the PVA-starch phantom.

3.2 Comparison of the homogeneity in dependence of the phantom material

Tables 1, 2 show the coefficients of variance (Cov) and the variations as defined in the EUREF protocol [39] for the three different phantom materials (PVA, PVA with starch, and PVA with microspheres) at three penetration depths (6, 8, and 10 cm) for two focal positions (top and middle).

No significant differences were found comparing the reference phantom with the other phantoms individually for the three depths nor comparing the averages of the reference phantom with the values of the other phantoms over all depths (Wilcoxon tests, p -values range from 0.16 to 1, mean p -value is 0.5).

Figure 9 shows a typical RIO for each material. While the standard deviation is similar for each material ($\sigma_{reference-phantom} = 10.7, \sigma_{PVA-phantom} = 11.4, \sigma_{microcapsule-phantom} = 11.4, \sigma_{starch-phantom} = 12.7$), the signal (i.e., MPV) varies due to the different echogenicity ($MPV_{reference-phantom} = 59.8, MPV_{PVA-phantom} = 67.5, MPV_{microcapsule-phantom} = 122.3, MPV_{starch-phantom} = 156.0$).

4 Discussion

The detectability index used revealed the expected behavior across various test scenarios depending on the frequency utilized. When adjusting for greater penetration depths, the frequency must be reduced to mitigate attenuation effects, as the system has to reduce the main frequency for lower attenuation. This relationship

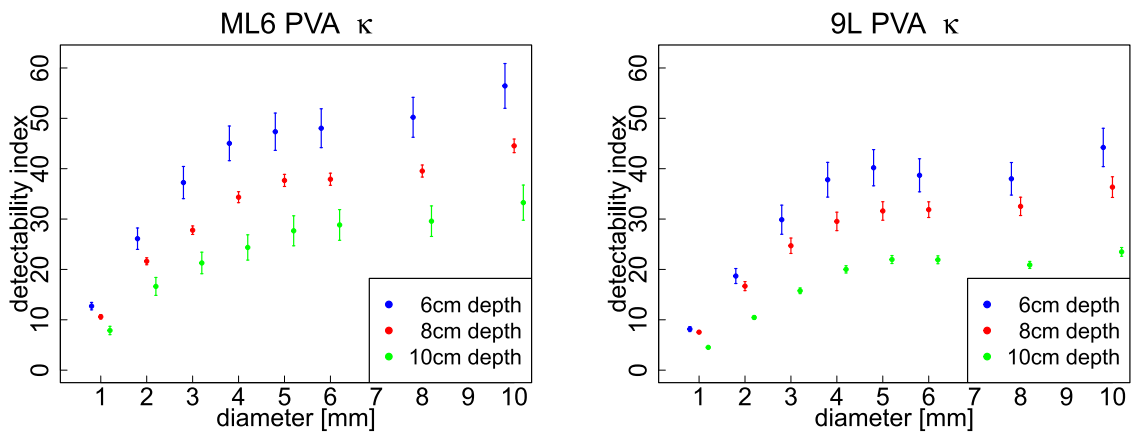


FIGURE 6 Detectability indices with ML6 and 9L transducers and PVA phantom. All values decrease with increasing penetration depth.

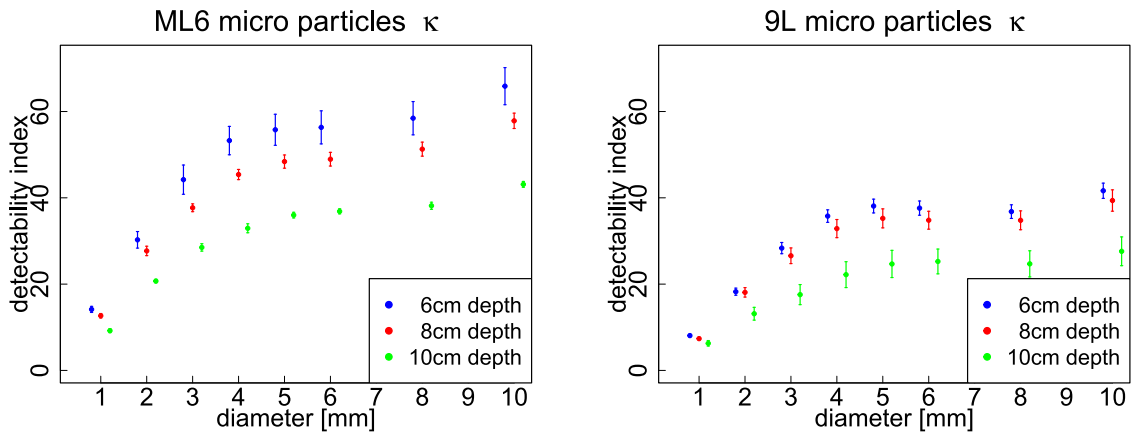


FIGURE 7 Detectability indices with the micro-sphere phantom.

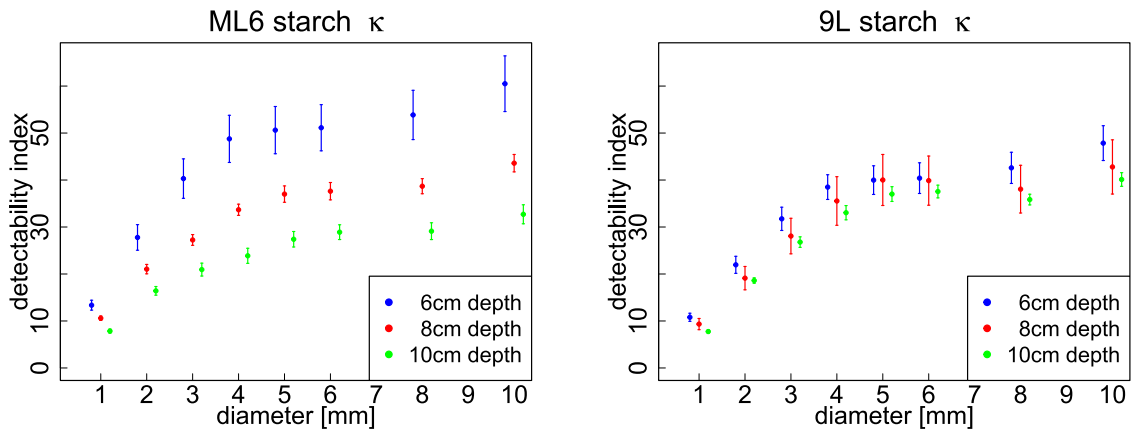


FIGURE 8 Detectability indices with the PVA-starch phantom.

TABLE 1 The variation of the bSNR of 3 different phantom materials in 3 penetration depths (6, 8 and 10 cm) within two image focus positions (top and middle).

Material	Focus position	6 cm	8 cm	10 cm
Reference phantom		0.16	0.17	0.16
PVA phantom	top	0.14	0.16	0.25
	mid	0.13	0.10	0.17
PVA starch phantom	top	0.20	0.23	0.04
	mid	0.22	0.15	0.33
PVA micro-sphere phantom	top	0.10	0.02	0.06
	mid	0.07	0.09	0.14

TABLE 2 The Cov in percent of the bSNR of different phantom materials in 3 penetration depths (6, 8 and 10 cm) within two image focus positions (top and middle).

Material	Focus position	6 cm	8 cm	10 cm
Reference phantom		5.61	6.08	5.39
PVA phantom	top	5.12	5.43	8.68
	mid	4.74	3.14	6.65
PVA starch phantom	top	6.67	8.03	1.55
	mid	8.38	5.52	9.96
PVA micro-sphere phantom	top	3.26	0.95	1.96
	mid	2.91	2.88	5.34

is also reflected in our results data: the greater the penetration depth, the lower the detectability index for all measurements. To cover the clinical range of application we positioned the (single) focus at a depth in the middle of the images. Furthermore, the index was consistently higher with the high frequency transducer 2 (ML6) compared to transducer 1 (9L), as expected from the theory.

These results can be translated to any clinical setting by computing the detectability index from the given κ when the distinct object to be detected is an anechoic structure such as a liquid in a vessel. Here, only the MPV of the background (e.g., the liver issue) has to be measured. Since the MPV of the liquid is assumed to be zero, the index is simply given by the product of κ and the measured MPV of the tissue. Potential improvements can then be quantified by comparing the index from different settings.

For further evaluation, the index needs to be calibrated and cross-checked with human readers using a contrast phantom to convert the index values to threshold diameters. This can be done using a calibration phantom as described in [40] which consists

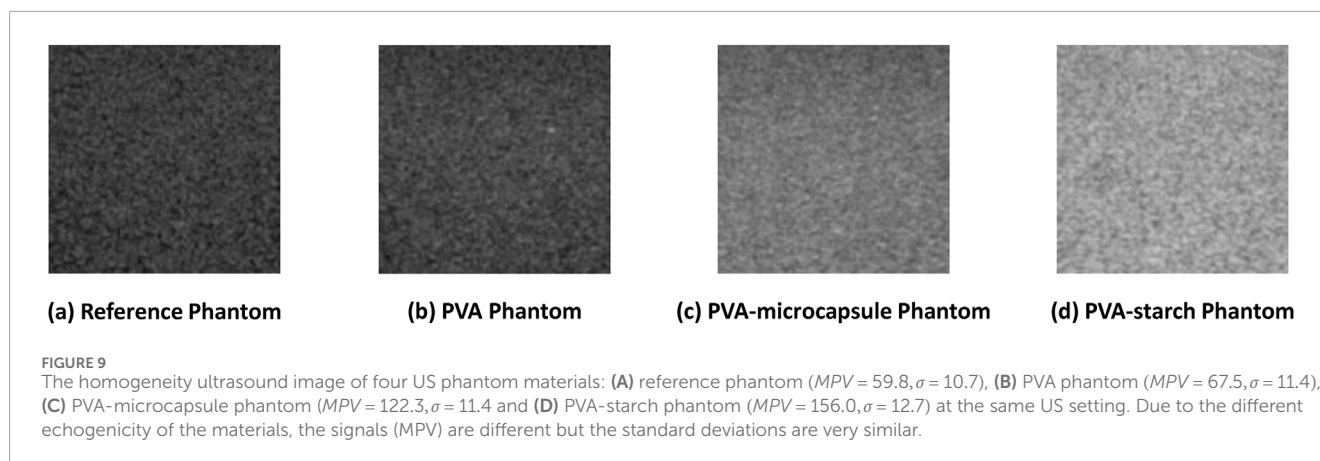
of cones made of different material compositions resulting in different echogenicities and therefore different MPVs in the images. By determining the smallest radius of the cone just visible in dependence of the contrast, a correlation can be derived from which the smallest just visible object can be determined given a calculated index. Once this has been achieved, our method can replace contrast-detail evaluation in existing quality assurance protocols [8].

The error bars (two sigmas) are relatively small, and the main source of error is due to the measurement of the NNPS. By establishing a single focal point, the range of homogeneous depth is approximately the same as that required to calculate the NNPS. Consequently, low-frequency components of the NNPS can be influenced by inhomogeneous components at the edge of the homogeneous region.

The homogeneity of the phantom material was similar for all phantoms and comparable to the commercial reference phantom. We have introduced a variation definition as it is used to evaluate the homogeneity of mammography images [39] where the limiting value is set to 0.10 to meet the standards. The X-ray imaging process generates smoother and adaptable noise, and therefore the homogeneity of mammography is expected to be much better than for US imaging. Therefore, we cannot use the same limiting value and had to determine the limiting value from commercial phantom. For both metrics, the homogeneity measures were in the same range as for the commercial phantom.

Our study has several limitations, firstly, the number of freeze-thaw cycles required during production affected the homogeneity of the phantom [32]. To create the homogeneous starch phantom, we mixed 10% PVA with 1% Lab starch and subjected it to several freeze-thaw cycles [23, 32]. Unfortunately, achieving homogeneity required at least four freeze-thaw cycles, which caused the phantoms to shrink and become smaller. Secondly, we found impurities in the PVA materials, contributing to the lack of phantom homogeneity. Microscopic examination of the PVA materials revealed the presence of metallic impurities mixed with the PVA materials. This impurity could have a significant impact on the manufacturing process and affect the overall homogeneity of the phantom [41]. Finally, there is the limitation of the proprietary materials used (PVA, starch, micro-sphere), where the constituents of these materials are not defined. It is difficult to precisely track back specific properties [42, 43], particularly the generated acoustic artifacts, back to the material composition. In addition, future studies should investigate the fabrication of contrast phantoms with different echogenicities and evaluate their physical properties and image quality [40]. By exploring different materials and compositions, we can better understand and optimize the performance of US phantoms for different applications [43, 44].

The newly introduced recipe using micro-spheres proved to be practical and gave satisfactory properties in terms of homogeneity. The superiority of this material over the others could theoretically be due to the possibility that these beads are also visible on MR and could therefore be used as phantom materials in hybrid US-MR applications. Unfortunately, the concentration of beads used was too low to be visible on MRI. On the other hand, increasing the concentration to the amount needed to produce a sufficient signal in MRI (about 20%) would result in too high US attenuation.



5 Conclusion and outlook

The results for the detectability index suggest that this concept can also be applied to US images. Using such concepts, standardized *objective* image quality assurance methods similar to those known from conventional x-ray imaging and mammography imaging can also be applied to medical US. As time-consuming subjective QA methods are currently used, this should facilitate routine QA evaluation.

We were able to produce different phantom materials with satisfactory homogeneity at the same noise level which was verified by the use of two established measures from [39]. As the materials had different MPVs, we were able to test our method for a variety of SNRs. We also presented a novel material composition for US phantoms, which incorporates core-shell micro-spheres filled with silicon oil of a viscosity of 10 cSt. This inclusion serves to enhance background scatter and increase the attenuation properties. We have also applied established X-ray image metrics to the US images, demonstrating their effectiveness in assessing image quality for US applications [43, 44].

A further development step for a possible US QA phantom applying the concept of a detectability index could include a three dimensional contrast detail phantom. With such a phantom the detectability indices could be calibrated to a human reader. By changing the material composition layer by layer in one direction, acoustic properties continuously vary in this direction, resulting in a varying signal. In the perpendicular direction the spatial frequency would be varied. The transducer plane is applied orthogonally which allows to define limit contrasts values and their conversion in detectability index thresholds.

Data availability statement

The original contributions presented in the study are included in the article/supplementary material, further inquiries can be directed to the corresponding author.

Author contributions

CS: Supervision, Validation, Visualization, Writing–original draft, Writing–review and editing, Conceptualization, Data curation, Formal Analysis, Funding acquisition, Investigation, Methodology,

Project administration, Resources, Software. JK: Writing–review and editing, Formal Analysis, Software. MO: Writing–review and editing, Data curation, Investigation, Resources. LZ: Writing–review and editing, Investigation. ES: Writing–review and editing, Methodology, Investigation. SH: Writing–review and editing, Investigation. PH: Supervision, Data curation, Formal Analysis, Investigation, Methodology, Validation, Writing–review and editing. CK: Writing–review and editing, Resources, Supervision, Data curation, Formal Analysis, Investigation, Validation. MF: Conceptualization, Data curation, Formal Analysis, Investigation, Methodology, Project administration, Resources, Software, Supervision, Validation, Visualization, Writing–review and editing. JH: Validation, Visualization, Writing–original draft, Writing–review and editing, Conceptualization, Data curation, Formal Analysis, Funding acquisition, Investigation, Methodology, Project administration, Resources, Software, Supervision.

Funding

The author(s) declare that financial support was received for the research, authorship, and/or publication of this article. This work was supported by the Austrian Research Promoting Agency (FFG) grants No. 861552 and No. 888047. Part of this research was supported by the M3dRES project infrastructure (Grant No. 858060), FFG. The financial support by the Austrian Federal Ministry for Digital and Economic Affairs, the National Foundation for Research, Technology and Development and the Christian Doppler Research Association is gratefully acknowledged.

Acknowledgments

The content of this manuscript has been presented in ultrasonic imaging and tomography at the SPIE Medical Imaging Conference 2024 [25].

Conflict of interest

The authors declare that the research was conducted in the absence of any commercial or financial relationships that could be construed as a potential conflict of interest.

Publisher's note

All claims expressed in this article are solely those of the authors and do not necessarily represent those of their affiliated

organizations, or those of the publisher, the editors and the reviewers. Any product that may be evaluated in this article, or claim that may be made by its manufacturer, is not guaranteed or endorsed by the publisher.

References

- Fry FJ. *Ultrasound: its applications in medicine and biology*. Elsevier (2013).
- Genovese M. Ultrasound transducers. *J Diagn Med Sonography* (2016) 32(1):48–53. doi:10.1177/8756479315618207
- Shung KK. Diagnostic ultrasound: past, present, and future. *J Med Biol Eng* (2011) 31(6):371–4. doi:10.5405/jmbe.871
- Rizzatto G. Ultrasound transducers. *Eur J Radiol* (1998) 27:S188–95. doi:10.1016/s0720-048x(98)00061-8
- Szabo TL, Lewin PA. Ultrasound transducer selection in clinical imaging practice. *J Ultrasound Med* (2013) 32(4):573–82. doi:10.7863/jum.2013.32.4.573
- Kirk Shung K, Zippuro M. Ultrasonic transducers and arrays. *IEEE Eng Med Biol Mag* (1996) 15(6):20–30. doi:10.1109/51.544509
- John Dudley N, James Woolley D, Stevenson MA. A survey of ultrasound quality assurance implementation in the United Kingdom. *Ultrasound* (2022) 30(4):308–14. doi:10.1177/1742271x221091713
- Kollman C, deKorte C, Dudley NJ, Gritzmman N, Martin K, Evans DH, et al. Guideline for Technical Quality Assurance (TQA) of ultrasound devices (B-Mode)-version 1.0 (July 2012): EFSUMB Technical Quality Assurance Group-US-TQA/B. *Ultraschall Med* (2012) 33:544–9. doi:10.1055/s-0032-1325347
- Hemmsen MC, Petersen MM, Ivanov Nikolov S, Nielsen MB, Jensen JA. Ultrasound image quality assessment: a framework for evaluation of clinical image quality. *Med Imaging 2010: Ultrason Imaging Tomography, Ther* (2010) 7629:105–16. doi:10.1117/12.840664
- Long Z, Tradup DJ, Stekel SF, Gorny KR, Hangiandreou NJ. Evaluations of ultraiq software for objective ultrasound image quality assessment using images from a commercial scanner. *J Appl Clin Med Phys* (2018) 19(2):298–304. doi:10.1002/acm2.12255
- Goodsitt MM, Carson PL, Witt S, Hykes DL, Kofler JM. Real-time b-mode ultrasound quality control test procedures. report of aapm ultrasound task group no. 1. *Med Phys* (1998) 25(8):1385–406. doi:10.1118/1.598404
- Jung JJ, Choi J-H, Hong Jung J. Image quality control for linear transducers with various frequencies by using an ats-550 phantom. *J Korean Phys Soc* (2017) 70(2):206–12. doi:10.3938/jkps.70.206
- Grazhdani H, David E, Ventura Spagnolo O, Buemi F, Perri A, Orsogna N, et al. Quality assurance of ultrasound systems: current status and review of literature. *J Ultrasound* (2018) 21:173–82. doi:10.1007/s40477-018-0304-7
- Culjat MO, Goldenberg D, Tewari P, Singh RS. A review of tissue substitutes for ultrasound imaging. *Ultrasound Med and Biol* (2010) 36(6):861–73. doi:10.1016/j.ultrasmedbio.2010.02.012
- Herzog M, Arsova M, Matthes K, Husman J, Toppe D, Kober J, et al. Technical assessment of resolution of handheld ultrasound devices and clinical implications. *Ultraschall der Medizin - Eur J Ultrasound* (2024) 45(04):405–11. doi:10.1055/a-2243-9767
- Young KC, Cook JJJ, Oduko JM, Bosmans H. Comparison of software and human observers in reading images of the cdmam test object to assess digital mammography systems. In: MJ Flynn, J Hsieh, editors. *Medical imaging 2006: physics of medical imaging*. SPIE (2006). doi:10.1117/12.653296
- Marshall NW. A comparison between objective and subjective image quality measurements for a full field digital mammography system. *Phys Med Biol* (2006) 51(10):2441–63. doi:10.1088/0031-9155/51/10/006
- Ng J, Prager R, Kingsbury N, Treece G, Gee A. Modeling ultrasound imaging as a linear, shift-variant system. *IEEE Trans Ultrason Ferroelectrics, Frequency Control* (2006) 53(3):549–63. doi:10.1109/tuffc.2006.1610563
- Bouhaouel F, Bauer F, Grosse CU. Task-specific acquisition trajectories optimized using observer models. In: 10th conference on industrial computed tomography (iCT 2020) (2020).
- Monnin P, Marshall NW, Bosmans H, Bochud FO, Verdun FR. Image quality assessment in digital mammography: part ii. npwe as a validated alternative for contrast detail analysis. *Phys Med and Biol* (2011) 56(14):4221–38. doi:10.1088/0031-9155/56/14/003
- Donini B, Rivetti S, Lanconelli N, Bertolini M. Free software for performing physical analysis of systems for digital radiography and mammography. *Med Phys* (2014) 41(5):051903. doi:10.1118/1.4870955
- Gang GJ, Tward DJ, Lee J, Siewerdsen JH. Anatomical background and generalized detectability in tomosynthesis and cone-beam ct. *Med Phys* (2010) 37(5):1948–65. doi:10.1118/1.3352586
- Kaar M, Semturs F, Figl M, Hoffmann R, Hummel J. Quality assurance for ultrasound scanners using a durable tissue-mimicking phantom and radial mtf. *Med Imaging 2014: Ultrason Imaging Tomography* (2014) 9040:353–9. doi:10.1117/12.2042476
- Strocchi S, Larghi F, Novario R. A quantitative method for the evaluation of spatial resolution in quality control of b-mode ultrasound images. *Ultrason Imaging* (2017) 40(2):113–26. doi:10.1177/0161734617741254
- Songaeng C, Salomon E, Ortner M, Zalka L, Köhrer J, Homolka P, et al. Determination of a detectability index for image quality evaluation using a pva-microcapsules phantom. In: N Bottenus, C Boehm, editors. *Medical imaging 2024: ultrasonic imaging and tomography*. SPIE (2024). doi:10.1117/12.3006046
- Sharma A, Geetha Marapureddy S, Paul A, Bisht SR, Kakkar M, Thareja P, et al. Characterizing viscoelastic polyvinyl alcohol phantoms for ultrasound elastography. *Ultrasound Med and Biol* (2023) 49(2):497–511. doi:10.1016/j.ultrasmedbio.2022.09.019
- Chen Y, Li J, Lu J, Ding M, Chen Y. Synthesis and properties of poly (vinyl alcohol) hydrogels with high strength and toughness. *Polym Test* (2022) 108:107516. doi:10.1016/j.polymertesting.2022.107516
- Bakry AM, Abbas S, Ali B, Hamid M, Mohamed YA, Ahmed M, et al. Microencapsulation of oils: a comprehensive review of benefits, techniques, and applications. *Compr Rev Food Sci Food Saf* (2016) 15(1):143–82. doi:10.1111/1541-4337.12179
- Paul S, Nahire R, Mallik S, Sarkar K. Encapsulated microbubbles and echogenic liposomes for contrast ultrasound imaging and targeted drug delivery. *Comput Mech* (2014) 53:413–35. doi:10.1007/s00466-013-0962-4
- O'Donnell PB, McGinity JW. Preparation of microspheres by the solvent evaporation technique. *Adv Drug Deliv Rev* (1997) 28(1):25–42. doi:10.1016/s0169-409x(97)00049-5
- van der Kooij RS, Steendam R, Frijlink HW, Hinrichs WLJ. An overview of the production methods for core-shell microspheres for parenteral controlled drug delivery. *Eur J Pharmaceutics Biopharmaceutics* (2022) 170:24–42. doi:10.1016/j.ejpb.2021.11.007
- Adelnia H, Ensandoost R, Moonshi SS, Gavani JN, Vasafi EI, Ta HT. Freeze/thawed polyvinyl alcohol hydrogels: present, past and future. *Eur Polym J* (2022) 164:110974. doi:10.1016/j.eurpolymj.2021.110974
- Samei E, Flynn MJ, Reimann D. A method for measuring the presampled MTF of digital radiographic systems using an edge test device. *Med Phys* (1998) 25(1):102–13. doi:10.1118/1.598165
- Erik F. Noise-power spectrum version 1.2.0.0 (2024). Available from: https://de.mathworks.com/matlabcentral/fileexchange/36462-noise-power-spectrum#version_history_tab (Accessed March 21, 2023).
- Barten PGJ. Physical model for the contrast sensitivity of the human eye. In: BE Rogowitz, editor. *Human vision, visual processing, and digital display III*. SPIE (1992).
- Borasi G, Samei E, Bertolini M, Nitrosi A, Tassoni D. Contrast-detail analysis of three flat panel detectors for digital radiography. *Med Phys* (2006) 33(6):1707–19. doi:10.1118/1.2191014
- Sipilä O, Blomqvist P, Jauhainen M, Kilpeläinen T, Malaska P, Mannila V, et al. Reproducibility of phantom-based quality assurance parameters in real-time ultrasound imaging. *Acta Radiologica* (2011) 52(6):665–9. doi:10.1258/ar.2011.100227
- Tsapaki V, Tsalafoutas IA, Triantopoulou SS, Triantopoulou C. Development and implementation of a quality control protocol for b-mode ultrasound equipment. *J Ultrasound* (2022) 25(2):155–65. doi:10.1007/s40477-021-00579-7
- van Engen R, van Woudenberg S, Bosmans H, Young K, Thijssen M. *European protocol for the quality control of the physical and technical aspects of mammography screening. Part 2b*. 4th ed France: European Breast Cancer Network Coordination

Office, International Agency for Research on Cancer (2006). F-69372 Lyon cedex 08.

40. Smith SW, Lopez H, Bodine WJ, Jr. Frequency independent ultrasound contrast-detail analysis. *Ultrasound Med and Biol* (1985) 11(3):467–77. doi:10.1016/0301-5629(85)90158-9
41. Zhu G, Ge M. Study on efficient degradation of polyvinyl alcohol in aqueous solution. *Environ Challenges* (2021) 4:100176. doi:10.1016/j.envc.2021.100176
42. Ammar AO. Performance evaluation of an ultrasonic imaging system using tissue-mimicking phantoms for quality assurance. *Biomimetics* (2022) 7(3):130. doi:10.3390/biomimetics7030130
43. Sassaroli E, Crake C, Scorza A, Kim D-S, Park M-A. Image quality evaluation of ultrasound imaging systems: advanced b-modes. *J Appl Clin Med Phys* (2019) 20(3):115–24. doi:10.1002/acm2.12544
44. Rownd JJ, Madsen EL, Zagzebski JA, Frank GR, Dong F. Phantoms and automated system for testing the resolution of ultrasound scanners. *Ultrasound Med and Biol* (1997) 23(2):245–60. doi:10.1016/s0301-5629(96)00205-0